

# Bachelor-Thesis

## Infrared Absorption Bands of Pure and Ho-doped Langasites

Alexander Weiser

alexander.weiser@outlook.at

Matr.Nr. 12102404

Date: November 11, 2024

Supervisors:

Univ.Prof. Dr. A. Pimenov, Dr. E. Constable

### Abstract

This study investigates the crystal electric field (CEF) spectrum of pure and holmium-doped langasite (p-LGS and Ho-LGS) crystals in the range from  $2250\text{ cm}^{-1}$  to  $21600\text{ cm}^{-1}$ , using FTIR transmission spectroscopy at temperatures as low as 5 K. The CEF structure plays a fundamental role in defining the ground state of rare-earth ions, directly influencing the magnetic and magnetoelectric (ME) properties unique to this system. Understanding the CEF spectrum is essential to advancing theoretical models and gaining insight into the electronic structure of rare-earth-substituted langasites.

Results reveal that Ho substitution significantly alters the optical and ME behavior of the crystal. In the mid-infrared range, observed absorption features are present in both pure and Ho-doped LGS, suggesting that these features are not caused by the Ho substitution. However, in the near-infrared range, Ho-LGS displays additional optical activity consistent with CEF transitions.

This initial survey of CEF spectra in langasites enhances the understanding of the optical properties of rare-earth-doped crystals, providing a foundation for the development of materials in advanced optical devices, such as optical diodes.

## Contents

<b>1</b>	<b>Introduction</b>	<b>3</b>
<b>2</b>	<b>Methods</b>	<b>5</b>
<b>3</b>	<b>Results</b>	<b>10</b>
<b>4</b>	<b>Discussion</b>	<b>20</b>
<b>5</b>	<b>Conclusion</b>	<b>22</b>
	<b>Figures</b>	<b>23</b>

<b>References</b>	<b>23</b>
<b>Appendix</b>	<b>24</b>

## 1 Introduction

Langasites ( $L_3Ga_5SiO_{14}$ , LGS) are emerging as promising materials due to their notable optical properties and strong piezoelectric and magnetoelectric (ME) effects. The non-centrosymmetric trigonal crystal structure of langasites ensures significant piezoelectric properties with high thermal stability [4]. Belonging to the P321 space group, this structure features threefold rotational symmetry along the  $c$ -axis and twofold rotation symmetry along the  $a$ - and  $b^*$ -axes, resulting in a lack of spatial inversion symmetry. The crystal consists of two alternating layers stacked along the  $c$ -axis, each possessing threefold symmetry, as illustrated in Fig. 1 below [2].

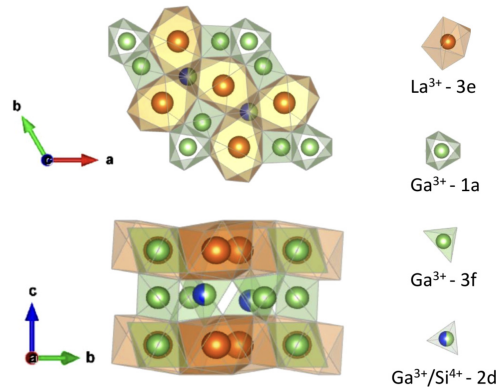


**Fig. 1:** P321 Crystal structure of langasite, adapted from Ref. [2].

An essential factor influencing the electronic and magnetic behavior of langasites is the crystal electric field (CEF). The CEF arises from the surrounding charge distribution of neighboring atoms within the crystal, which breaks the degeneracies of electronic orbitals for ions within the lattice. This splitting defines the ground state of ions, making the CEF crucial for understanding magnetic and magnetoelectric (ME) properties.

In langasites, substituting rare-earth (RE) ions partially for lanthanum (La) adds unique optical properties to the system. Rare-earth elements like holmium (Ho) possess unpaired  $f$ -electrons, which are strongly influenced by the CEF. In Ho-doped langasites (Ho-LGS), the CEF splits the electronic states of the  $f$ -orbitals into sub-levels, effectively creating a new set of electronic energy levels. These levels contribute significantly to the material's magnetic and ME properties.

The inclusion of magnetic ions within the langasite lattice, combined with its piezoelectric properties, results in complex magnetic structures and unusual ME effects [6].

The crystal's threefold symmetry may promote magnetic frustration, leading to ME effects even in the absence magnetic order. In the disordered paramagnetic state of Ho-doped langasite, a combination of linear and nonlinear ME responses features novel electric polarization behavior [2, 7].

Langasites also exhibit strong dielectric anisotropy, with the permittivity along the  $c$ -axis being significantly higher than along the twofold axes [2].

Considering the unique ME properties of systems like Ho-LGS, langasite emerges as a strong candidate for non-reciprocal dichroism (NRDC), which originates from the coupling between electric and magnetic dipoles in ME materials. The absence of both spatial inversion and time-reversal symmetry enables the absorption of light to differ depending on the direction of propagation, effectively forming an optical diode (OD). This capability is especially valuable for applications in fields such as life sciences and telecommunications, particularly in the near-infrared

range [3].

To gain a deeper understanding of the CEF structure, which influences these magnetic and ME effects, it is essential to probe the spectrum of electronic states directly. Infrared spectroscopy offers a powerful approach for exploring crystal field effects by capturing the energy levels and transitions affected by this field. Such insights into the electronic ground states are crucial for informing further theoretical developments.

This work presents an initial survey of the CEF spectra of pure LGS and Ho-doped LGS across a temperature range from 5 K to 300 K. The study covers a spectral range from near-infrared to mid-infrared ( $500 - 22500 \text{ cm}^{-1}$ ), enabling a broad-band probe of the CEF spectrum and allowing observation of changes induced by Ho substitution. This investigation aims to contribute to the understanding of a promising class of materials, ultimately advancing the development of optical diodes and facilitating non-reciprocal control of light in emerging technological applications [3].

## 2 Methods

In the following study, two langasite crystal samples were investigated: a pure  $\text{La}_3\text{Ga}_5\text{SiO}_{14}$  (p-LGS) crystal and a partially substituted Holmium-langasite  $(\text{Ho}_x\text{La}_{1-x})_3\text{Ga}_5\text{SiO}_{14}$  (Ho-LGS) with  $x = 0.05$ . Both samples were mechanically polished on surfaces perpendicular to the a-axis (a-cut) and had a surface area of approximately  $5 \times 5 \text{ mm}^2$  [2]. The thickness of the p-LGS sample was measured using an analog caliper and found to be  $2.0 \pm 0.05 \text{ mm}$ , while the thickness of the Ho-LGS sample was labeled on the sample box as  $2.934 \pm 0.05 \text{ mm}$  and was confirmed. The Ho-LGS sample contains a crack in the a-b plane, whereas the p-LGS sample showed no visible defects.

The transmittance in the infrared range from  $300 - 26\,000 \text{ cm}^{-1}$  was measured using a *Bruker Vertex 80v* Fourier-Transform-Infrared (FTIR) spectrometer. Due to the broad spectrum, the measurements were split into three frequency groups, each with different system settings, as listed in the table below:

	Range ( $\text{cm}^{-1}$ )	Beamsplitter	Detector	Polarizer	Source of Light
NIR	8000 - 26000	$\text{CaF}_2$	SiDiode	NIR	Tungsten Lamp
NMIR	2000 - 12000	$\text{CaF}_2$	DLaTGS	NIR	Tungsten Lamp
MIR	300 - 8000	$\text{KBr}$	DLaTGS	MIR	Globar

**Tab. 1:** System Settings of *Bruker* FTIR spectrometer.

In addition, the scanning resolution was set to  $10 \text{ cm}^{-1}$  and the source aperture to 2 mm. The entire system was evacuated during the measurements to minimize absorption caused by air humidity.

Since measurements were taken at temperatures ranging from 5 K to 300 K, the samples were mounted on a He-flow cryostat. The temperature was controlled by circulating liquid helium and using an external heating device. Inside the cryostat, an external vacuum pump maintained a pressure of approximately  $10^{-6} \text{ mbar}$ . For the cryostat, KBr windows were chosen because of their consistent transparency across the entire observed spectrum. Additionally, an aluminum shielding was attached to reduce thermal radiation. Both crystals were mounted on the copper plate of the cryostat at apertures of approximately 2 mm using sticky tin foil, which is reliable at low temperatures. An additional empty aperture served as a reference. The samples were mounted with the polished surface facing outward, so that the a-axis protruded orthogonally, while the c-axis remained parallel to the cryostat, as shown in Fig. 2.

Before the cryostat, a rotatable polarization filter (polarizer) was placed in the sample compartment of the spectrometer. The filter was adjusted so that when aligned at  $0^\circ$ , the electric field  $\vec{E}$  was vertically polarized, making it parallel to the c-axis ( $\vec{E} \parallel c$ ). When aligned at  $90^\circ$ , the electric field  $\vec{E}$  was horizontally polarized, making it orthogonal to the c-axis ( $\vec{E} \perp c$ ).

The basic analysis of the FTIR transmission spectra was performed using *Python*. Transmission was calculated by dividing the intensity of the sample measurement  $I_{\text{sample}}$  by the intensity of the reference measurement  $I_{\text{reference}}$ , apparent in Fig. 2, using the formula:

$$T = \frac{I_{\text{sample}}}{I_{\text{reference}}}. \quad (1)$$

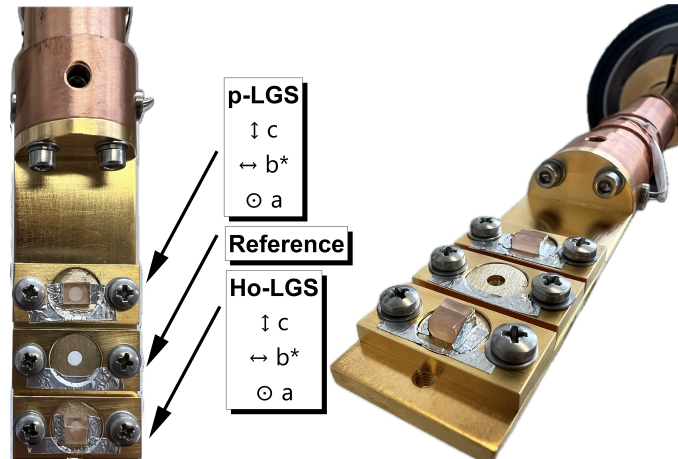


**Fig. 2:** Samples on Cryostat-Sample-Stick with Axis Label.

The data from the three spectral ranges were then segmented and concatenated. Due to significant noise at the edges, the ranges were qualitatively defined as MIR [500; 4000] (mid-infrared), NMIR (4000; 8800) (near-mid-infrared), and NIR [8800; 22500] (near-infrared) (in  $\text{cm}^{-1}$ ).

At the boundaries of these ranges, discontinuities in the data were observed. To address this, an additional measurement was conducted without samples, using the same system settings and setup at room temperature. This test revealed how different system configurations and the cryostat's position influenced the transmission. As shown in Fig. 3, the middle range (NMIR) yielded the most reliable measurements. Consequently, the MIR and NIR portions of each file were shifted accordingly to produce a smooth spectrum.

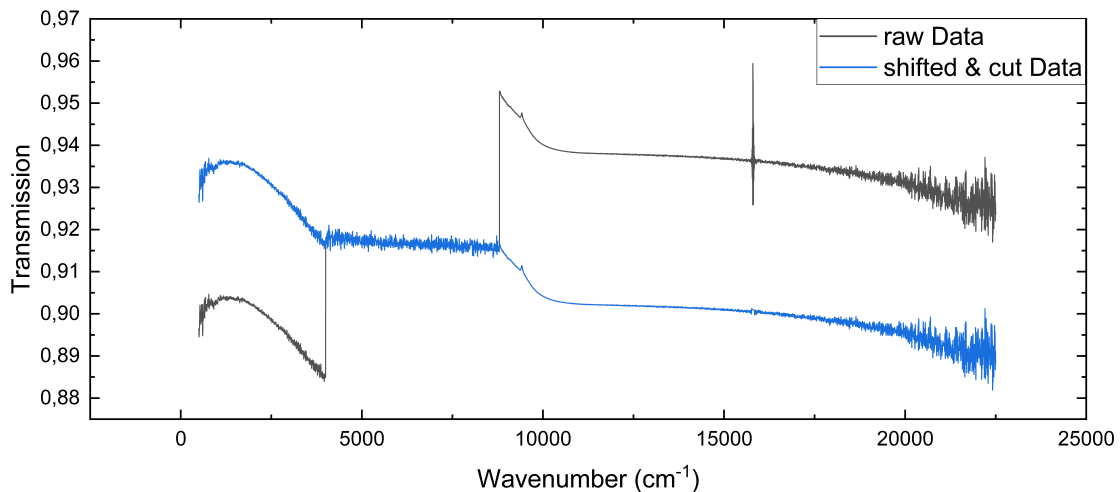


**Fig. 3:** Transmission Reference of Bottom Place (Ho-LGS) at Room Temperature and with  $\vec{E} \perp c$ .

Additionally, it is expected that the deviations observed in the reference measurements (which ideally should be constant at the value 1) also appear in the previously measured transmission of the sample. To account for this, the transmission spectra of the samples were divided by the corresponding reference spectra taken without the samples. The uncertainty of the sample measurement is expected to match that of the system reference, and since the sample data is

divided by the reference, the error propagation results in doubling the uncertainty.

To improve the accuracy of the uncertainty, the interference from the system's scanning HeNe laser (measured at  $15799.28 \text{ cm}^{-1}$  in the spectra) was removed from the reference spectrum. The uncertainty was then calculated as the standard deviation, which amounted to:

p-LGS:	$\vec{E} \parallel c$	0.00949
	$\vec{E} \perp c$	0.02512
Ho-LGS:	$\vec{E} \parallel c$	0.03501
	$\vec{E} \perp c$	0.02495

**Tab. 2:** Standard Deviation of  $\pm 1\sigma$  for Transmission Spectra.

The (Napierian) attenuation coefficient  $\alpha$  can be derived from the Beer-Lambert law for a homogeneous medium [5]:

$$T = \frac{I_{\text{sample}}}{I_{\text{reference}}} = e^{-\alpha d}, \quad (2)$$

$$\alpha = -\frac{\ln T}{d}, \quad (3)$$

where  $d$  is the thickness of the sample and  $T$  is the transmission. The uncertainty in  $\alpha$  can be expressed as:

$$\begin{aligned} \sigma_{\alpha} &= \sqrt{\left(\frac{\partial \alpha}{\partial T}\right)^2 \sigma_T^2 + \left(\frac{\partial \alpha}{\partial d}\right)^2 \sigma_d^2} \\ &= \sqrt{\left(-\frac{1}{T \cdot d}\right)^2 \sigma_T^2 + \left(\frac{\ln T}{d^2}\right)^2 \sigma_d^2}. \end{aligned} \quad (4)$$

The thickness of the p-LGS sample is 0.002 m and for the Ho-LGS crystal, it is 0.002934 m, with an uncertainty of  $\sigma_d = 0.00005$  m, as mentioned earlier in this chapter.

Further peak analysis of the attenuation coefficient spectrum was conducted using *OriginPro* software. To establish an appropriate baseline, for each sample and polarization, anchor points were manually set (see Tab. 5) and connected using spline interpolation. This method produced the best results. By subtracting this baseline, the data was prepared for peak fitting, as shown in Fig. 4.

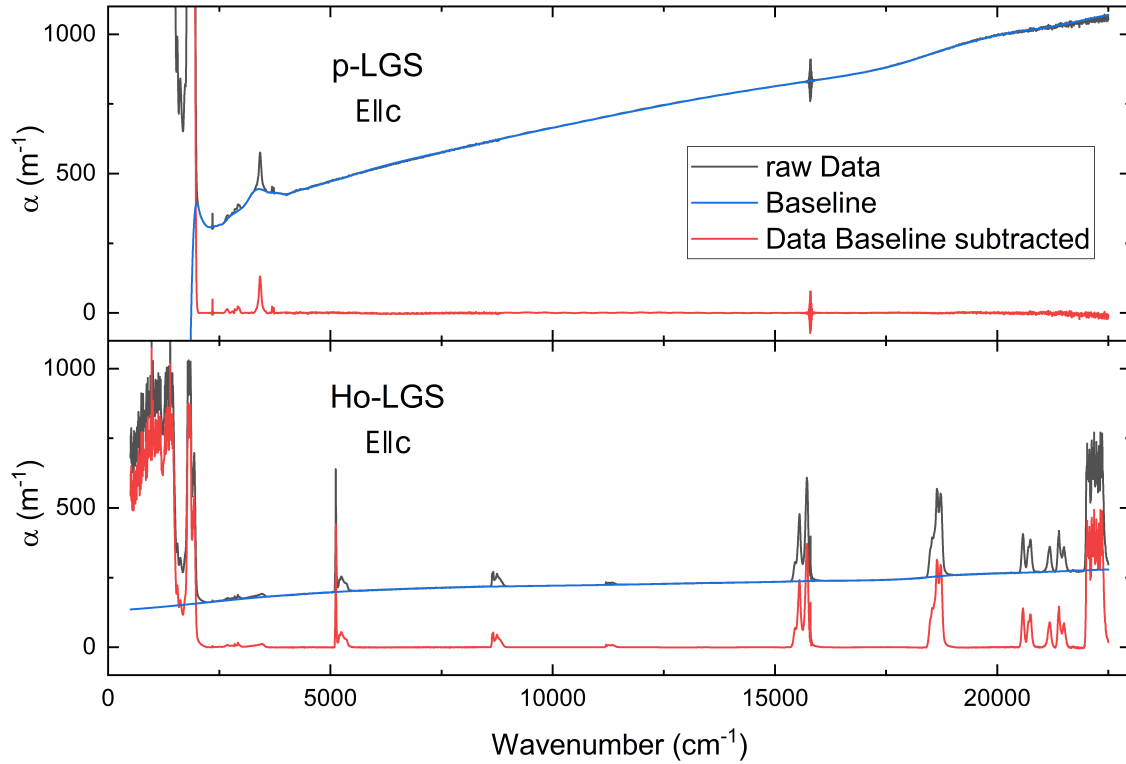


**Fig. 4:** Baseline Subtraction of p-LGS and Ho-LGS at 5K.

Since there is significant noise at the beginning and end of the spectrum, only frequencies between  $2250 - 21600 \text{ cm}^{-1}$  were considered in the peak analysis. For each of the four attenuation spectra the peaks were initialized at 5 K and from that the peak behavior as a function of temperature investigated. Only peaks that are (positive) local maximums, with a resolution of  $20 \text{ cm}^{-1}$  and a minimum threshold height of  $5 \text{ m}^{-1}$  were chosen. In the spectrum of p-LGS the significant peak of the scanning laser was excluded. Hence, the initial peak indices vary throughout the different spectra. In Tab. 3, the wavenumbers of all initial peaks are listed. Peaks representing the same feature in different spectra but assigned different indices are highlighted in the same color.

Peak Index	Ho-LGS		p-LGS	
	$\vec{E} \parallel c$	$\vec{E} \perp c$	$\vec{E} \parallel c$	$\vec{E} \perp c$
1	2346.099	2346.099	2347.545	2347.545
2	2677.330	2683.115	2671.544	2680.222
3	2797.383	2848.008	2795.936	2848.008
4	2848.008	2915.989	2849.454	2927.561
5	2915.989	3417.898	2914.543	3416.452
6	3464.184	5121.785	3416.452	3688.379
7	5120.339	5256.302	3688.379	3725.986
8	5238.945	8635.147	3725.986	
9	8661.183	8694.451		
10	8745.075	8779.790		
11	11196.763	11238.709		
12	11273.423	11338.512		
13	11341.405	15452.140		
14	15452.140	15553.390		
15	15551.944	15711.050		
16	15716.836	15799.282		
17	15799.282	18577.861		
18	18535.915	18642.950		
19	18642.950	18732.628		
20	18723.950	20576.818		
21	20578.265	20712.782		
22	20747.496	21182.870		
23	21175.637	21386.815		
24	21386.815	21493.851		
25	21502.529			

**Tab. 3:** Peak Frequencies in  $\text{cm}^{-1}$  at 5K.

However, when discussing the results in Ch. 3, new indices will be assigned to ensure clarity.

### 3 Results

As one can already see from the not-yet-baseline-corrected full transmission spectra in Fig. 5, the two crystals display similar background trends but differ significantly in their absorption spectra.

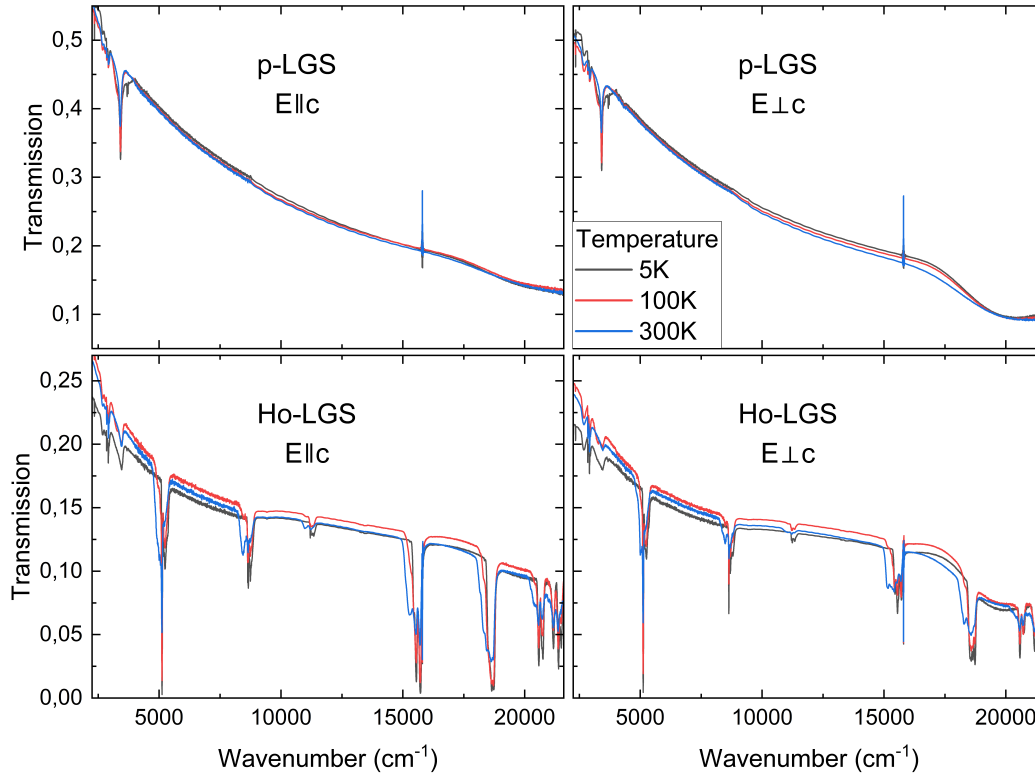


**Fig. 5:** Full Transmission Spectra.

By calculating the attenuation coefficient  $\alpha$  and applying baseline correction (resulting in  $\Delta\alpha$ ), the intensity of absorption peaks can be analyzed more precisely across the full attenuation-coefficient spectrum (Fig. 6). New peak indices were assigned to categorize peak groups that appear in multiple crystals or polarizations. However, the prominent peak from the system's scanning HeNe laser at approximately  $15799\text{ cm}^{-1}$ , present in all spectra, was disregarded as it represents a system artifact rather than a physical property of the crystal. Notably, the Ho-doped langasite exhibits extensive optical activity starting from  $4800\text{ cm}^{-1}$ , whereas the pure langasite does not display any interaction at these frequencies.

To interpret the behavior of the peaks as a function of temperature, each peak was fitted using *OriginPro* software, with the fitting initialized at 5 K. This approach captures the most accurate representation of how the peaks grow or diminish as the temperature increases. However, if new peaks emerge at higher temperatures, they are not included in this dataset, although they should still be visible in the graphs. Each peak was characterized by a Gaussian function, with its amplitude, peak frequency, and full width at half maximum (FWHM) defined — though the FWHM values occasionally showed imprecise or scattered results.

The systems of pure langasite (pure-LGS) and Ho-doped langasite (Ho-LGS) are structurally very similar, as the substitution of  $\text{Ho}^{3+}$  for  $\text{La}^{3+}$  is only around 5%. Therefore, the phonon modes are expected to remain nearly identical in both systems, given that phonon behavior primarily depends on the lattice structure and atomic masses, which are minimally affected by

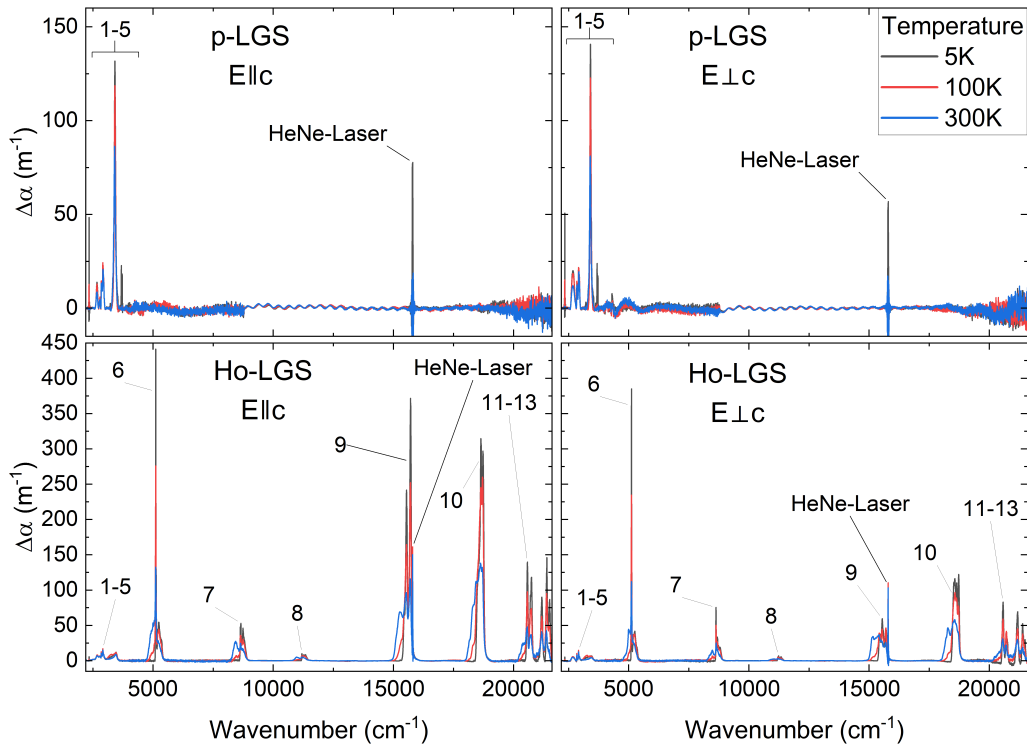


**Fig. 6:** Full Attenuation-Coefficient Spectra.

this small doping level. However, the presence of f-electrons in the rare-earth  $\text{Ho}^{3+}$  ions introduces additional electronic transitions unique to the doped system. In Ho-LGS, the crystal electric field (CEF) influences these f-orbitals by splitting the f-electron energy levels. Transitions between these split sub-levels, known as CEF excitations, also contribute to the absorption spectrum.

In the observed spectrum, CEF electronic transitions are anticipated to be the primary contributor to the absorption behavior, as phonon modes typically occur at lower frequencies [2]. These transitions follow the Boltzmann distribution, which describes the population of energy states as a function of temperature or energy. In a two-state system approximation, the absorption peak amplitude  $A$  is proportional to the population difference between the excited state  $N_2$  and the ground state  $N_1$ , represented by  $A(T) \propto N_1 - N_2 = N_1(1 - e^{-\frac{\Delta E}{kT}})$ , where a larger energy difference between the two states results in a more gradual exponential decrease in amplitude with temperature.

Conversely, the population of phonon modes at low temperatures is described by the Bose-Einstein distribution, which increases with temperature. However, at higher temperatures, damping effects and anharmonic interactions, such as thermal broadening, dominate, leading to a reduction in amplitude.

With increasing temperature, thermal expansion of the crystal can cause slight frequency shifts for both electronic and phonon-related absorption peaks. However, phonons are more susceptible to interactions, resulting in a more pronounced downward shift in frequency.

At the beginning of the observed spectrum, within the frequency range of  $2300 - 3700 \text{ cm}^{-1}$ , the absorption spectra of Ho-LGS exhibits a structure very similar to that of pure-LGS, as illustrated in Fig. 7. Generally, Ho-LGS shows weaker absorption compared to pure-LGS; however, there is

almost no change in intensity between the different polarizations. The peak parameters of the corresponding peaks are presented in Fig. 8, enabling a detailed interpretation of peak behavior.

The peaks within Group 3 display a slight, almost constant decrease in amplitude with increasing temperature, which may suggest electronic transitions from states possibly close to the ground state. Peak 1, however, demonstrates a low-temperature activation, suggesting a small energy splitting between two states. Peak 4 shows a moderate decrease in amplitude, still indicative of electronic transitions. Across all discussed peaks, the frequency remains relatively constant, within the margin of error.

The unique appearance of Peaks 5a & 5b at only very low temperatures in pure-LGS could be attributed to impurities within the crystal.

Given the notably similar structure of the absorption spectra between the two crystals, Peaks 1–4 likely do not arise from electronic transitions associated with the substitution of Ho but rather from other elements within the crystals, such as La, Ga, Si or O.

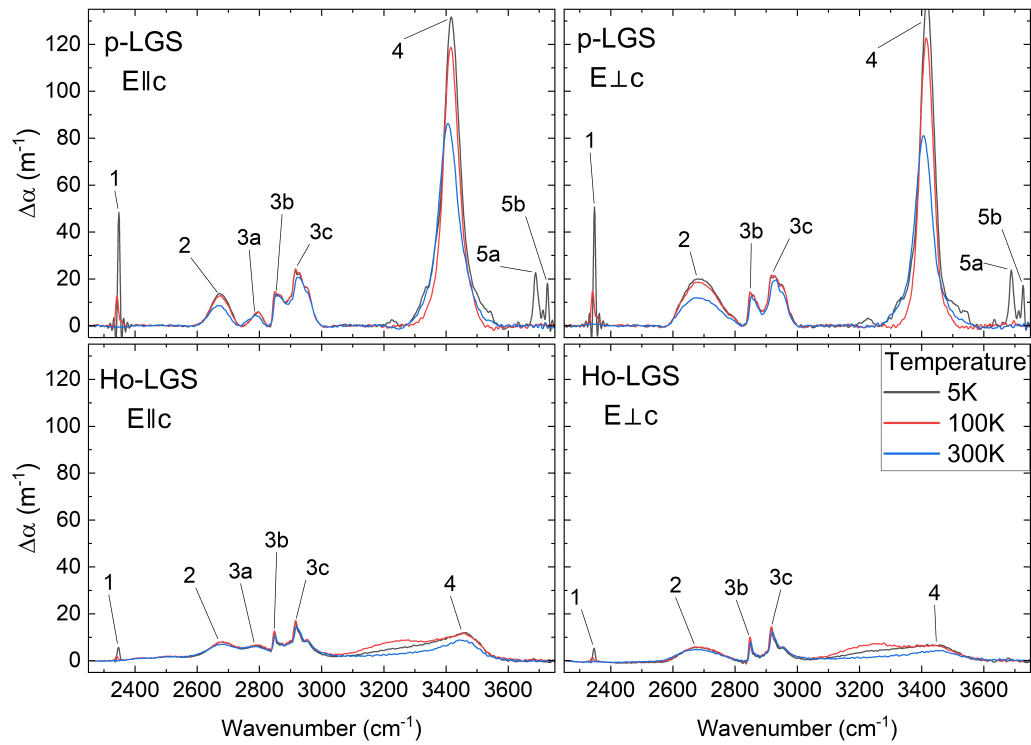


**Fig. 7:** Attenuation-Coefficient for 2300 - 3700  $\text{cm}^{-1}$ .

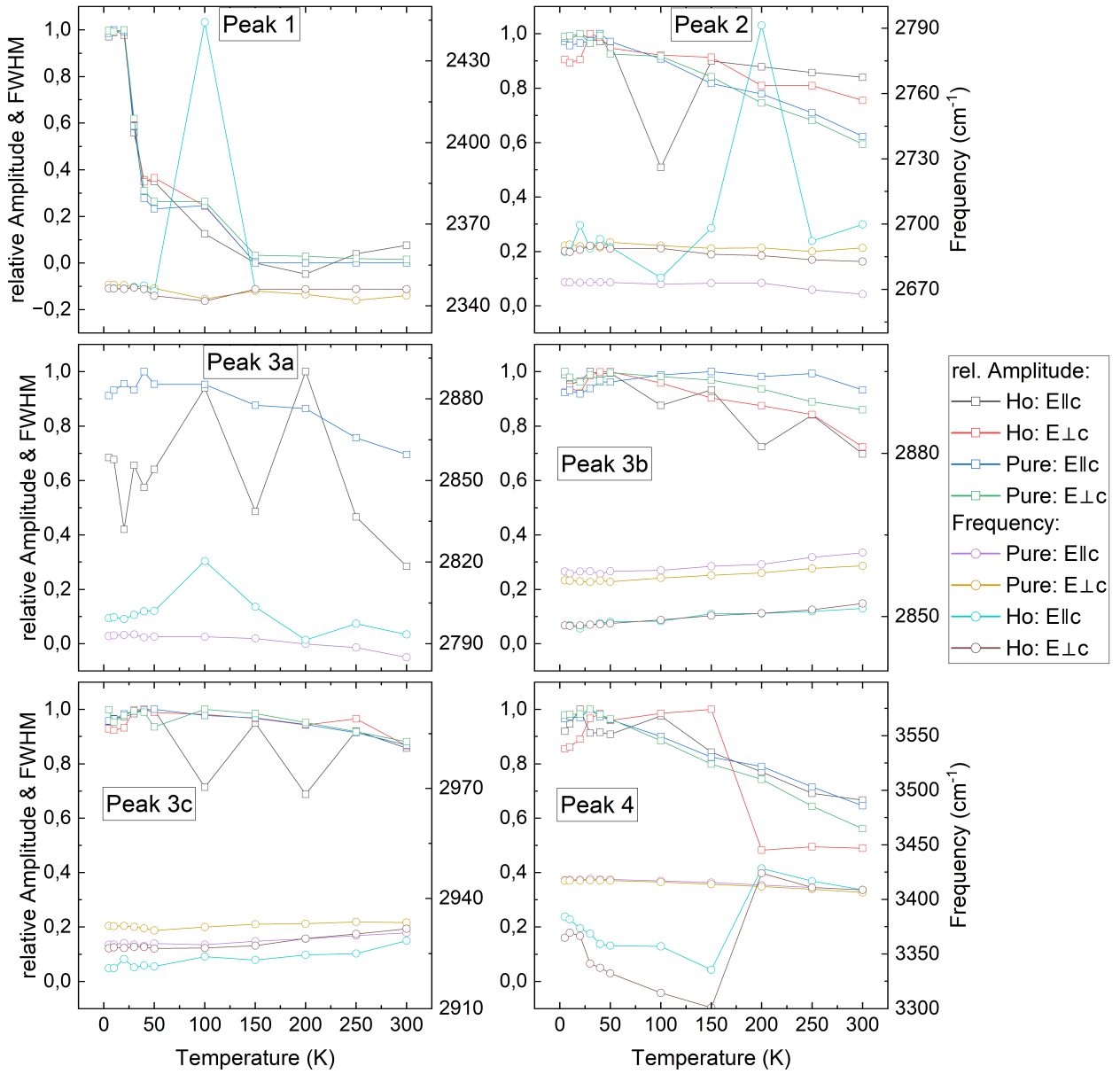


**Fig. 8:** Parameters for Peak 1, 2, 3a, 3b, 3c & 4.

From frequencies of around  $4800\text{ cm}^{-1}$  onward, the absorption spectra of Ho-LGS significantly differ from those of pure-LGS, showing numerous optical excitations that are unique to the substituted system. The most remarkable absorption feature is Peak 6. Fig. 9 & 10 show this strong, sharp peak, which stands out relatively isolated from other spectral features. Notably, below a threshold temperature of approximately 50 K, all peak parameters behave differently than expected for typical electronic transitions. Specifically, there appears to be a slight saddle in the amplitude at this temperature and an increasing shift in the frequency.

Since there is no comparable peak in the spectrum of pure-LGS, a purely phonon-based interaction is not plausible. However, spin-lattice coupling may be a reasonable explanation for this behavior, although further verification is needed.

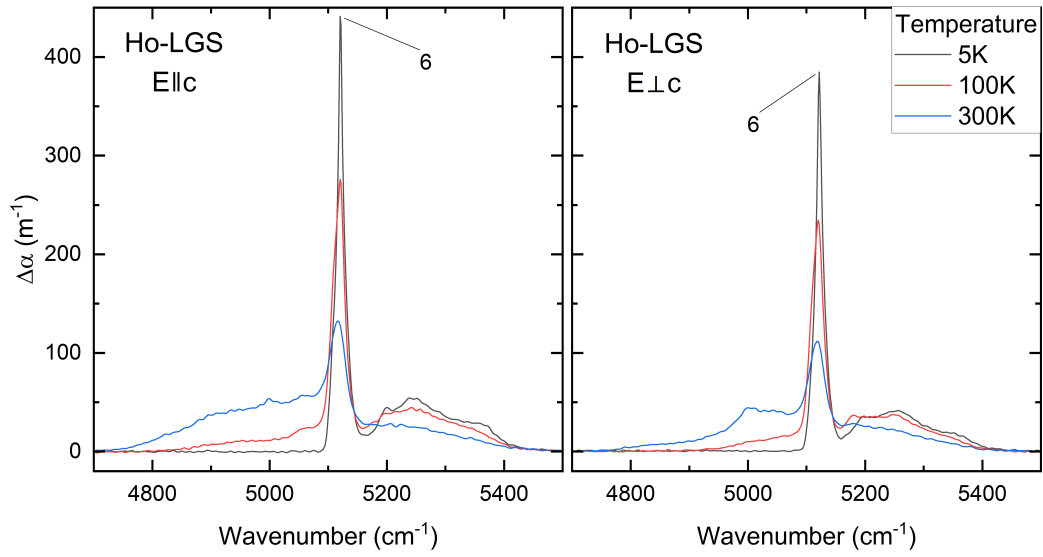


**Fig. 9:** Attenuation-Coefficient for 4800 - 5400  $\text{cm}^{-1}$ .

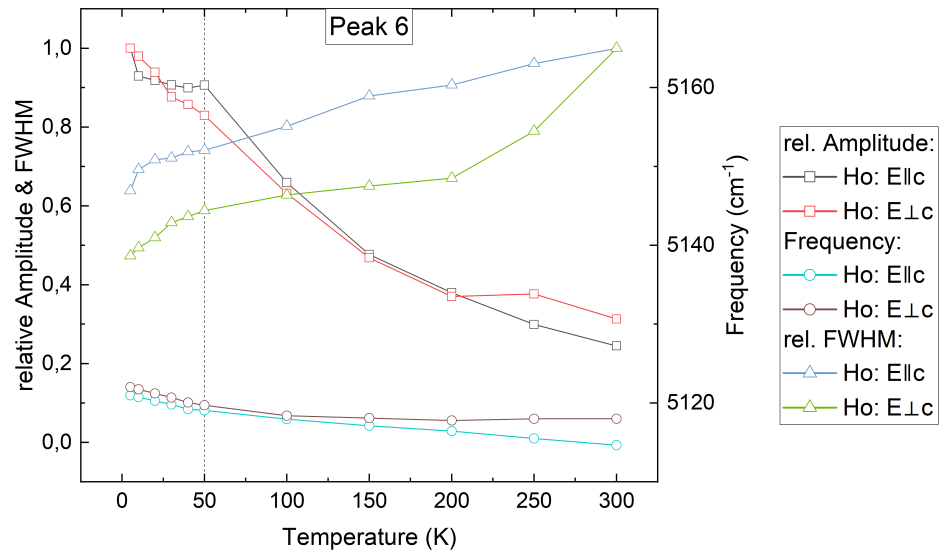


**Fig. 10:** Parameters for Peak 6.

The peaks in Groups 7 & 8, within the frequency range of 8000 - 11500  $\text{cm}^{-1}$ , exhibit complex behavior with temperature. Some peaks diminish with increasing temperature, while others emerge only at relatively high temperatures. These peaks appear to be an overlap of several individual transitions, which made the peak fitting challenging, and thus the fitted parameters may not be fully accurate. As shown in Fig. 11, the overall spectrum changes notably with temperature, suggesting some form of electronic population dependency.

Notably, many closely spaced single peaks contribute to the observed overlapped peaks, likely due to CEF excitations resulting from the small energy splitting of the f-orbitals. By comparing the peaks at 5 K and 300 K, it can be inferred that the peaks labeled 7 & 8 are likely indicative of the actual underlying energy levels.

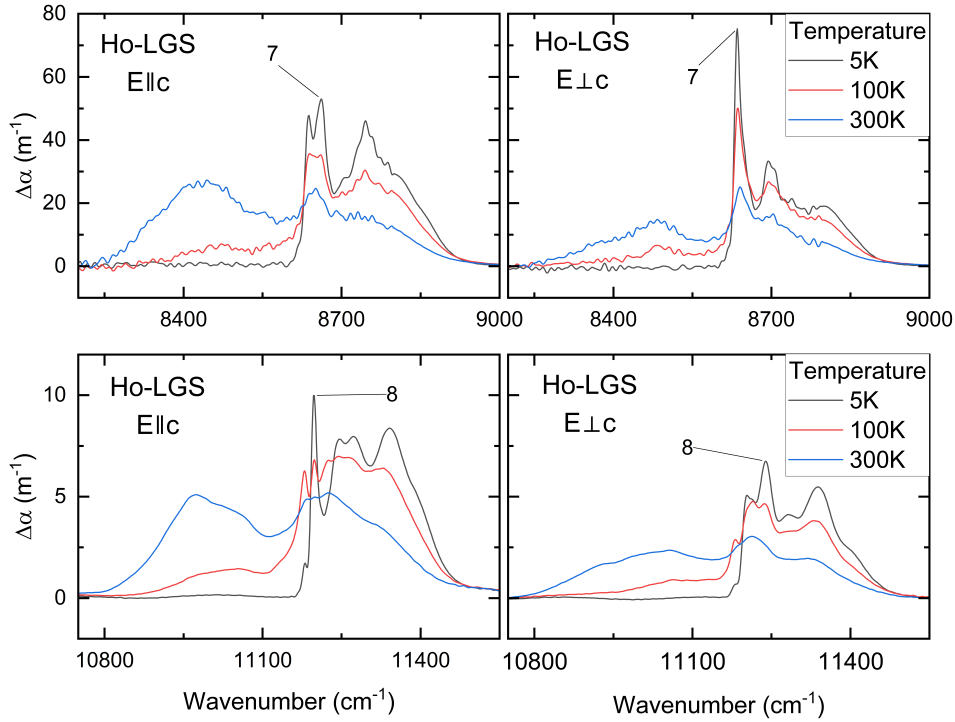


**Fig. 11:** Attenuation-Coefficient for 8000 - 11500  $\text{cm}^{-1}$ .

At higher frequencies, the absorption intensity varies with polarization, with the  $\vec{E} \parallel c$  configuration exhibiting stronger absorption than  $\vec{E} \perp c$ , as shown in Fig. 12. The relevant peak parameters are displayed in Fig. 13. In the frequency range of 14850 - 21600  $\text{cm}^{-1}$ , all 10 peaks show a significant decrease in absorption amplitude, following the Boltzmann distribution. Only Peak 9b deviates from this trend, showing an increase in amplitude at temperatures below 50 K, similar to Peak 6, where spin-lattice coupling may be assumed.

Peaks 9a, 9b, 13a & 13b exhibit a slightly larger shift in frequency compared to the others, though still within the range of error. The FWHM, while occasionally scattered, generally reflects the trend of peak broadening, with some exceptions for Peaks 10c & 11b. Overall, this behavior reflects normal thermal population dynamics of CEF excitations, suggesting that these peaks likely result from crystal field effects.

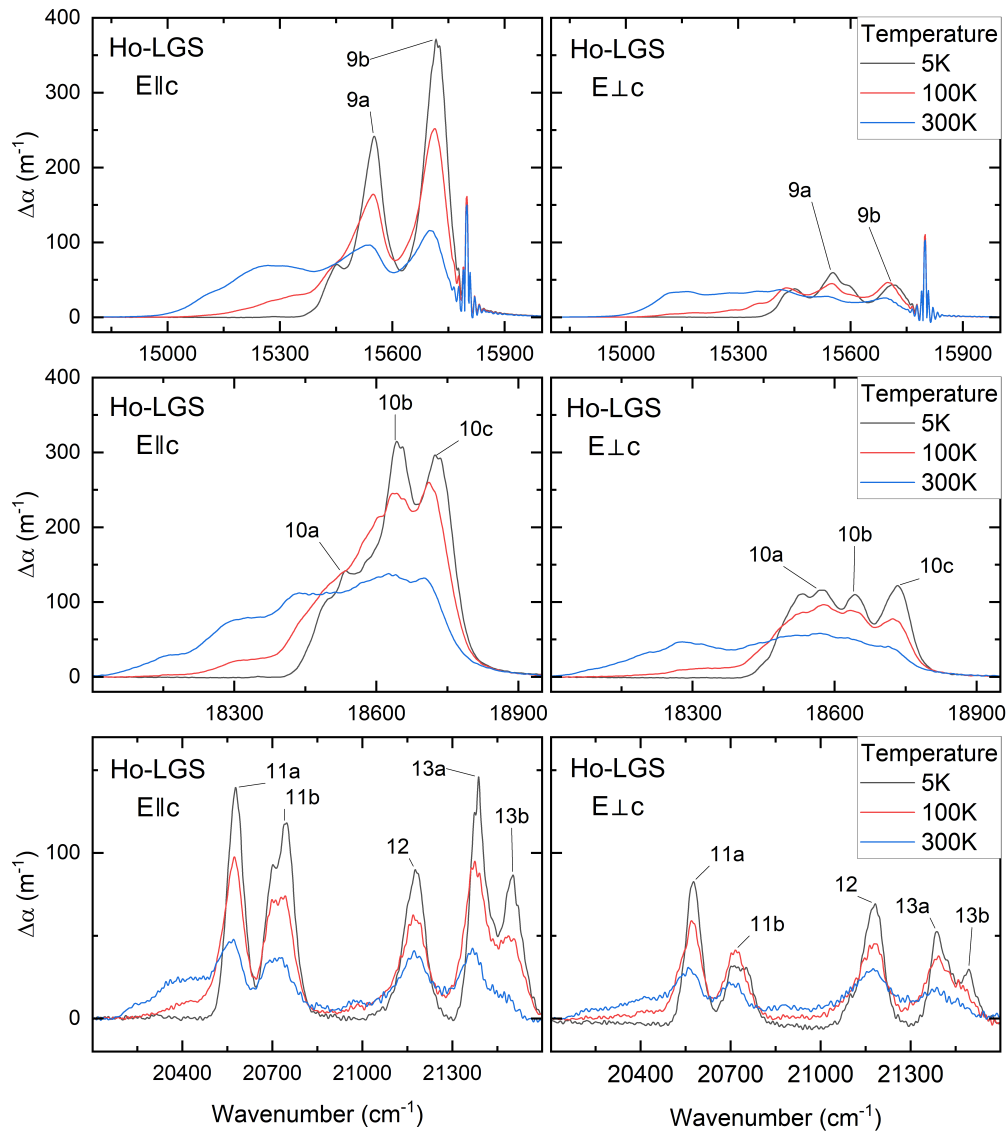


**Fig. 12:** Attenuation-Coefficient for 14850 - 21600  $\text{cm}^{-1}$ .

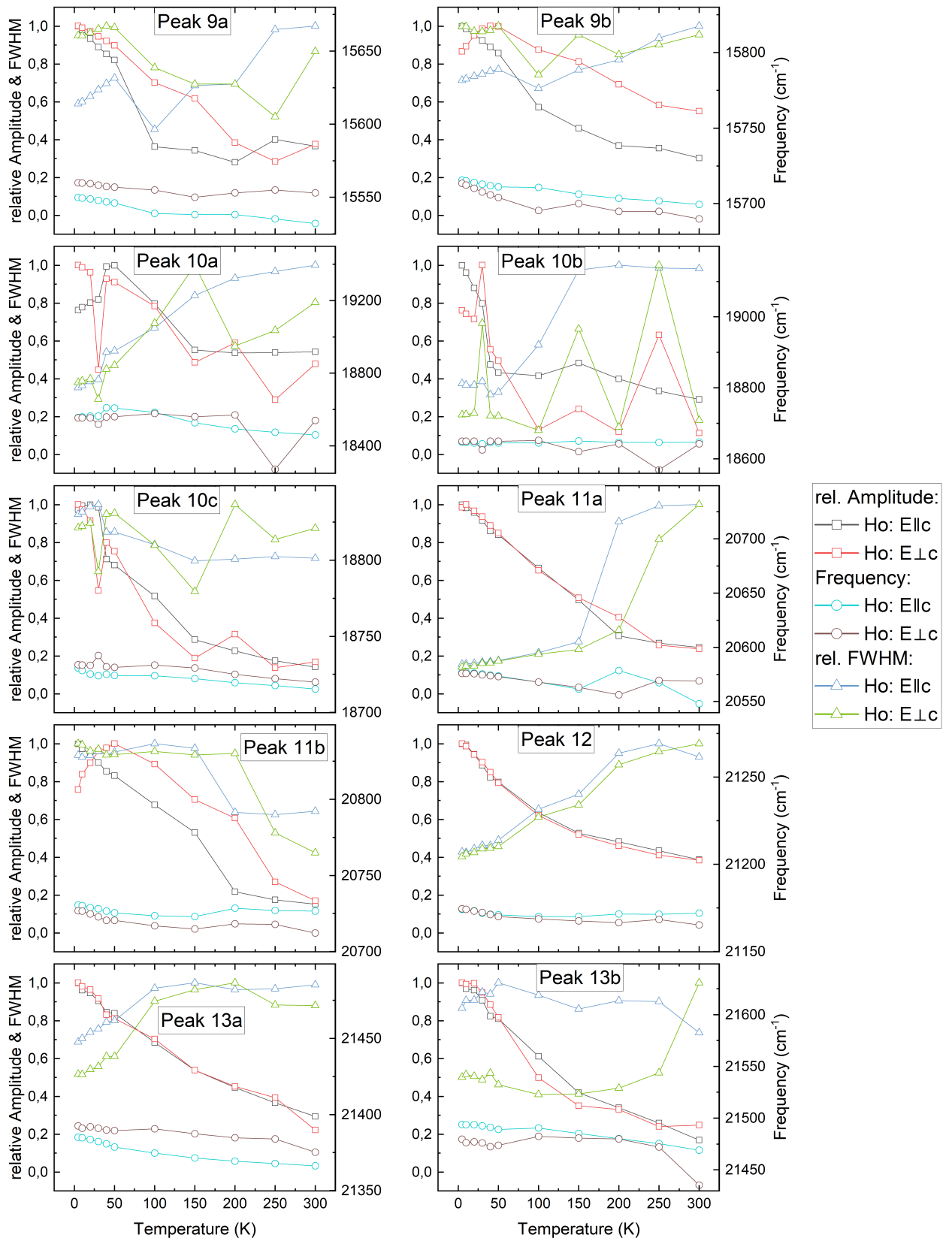


Fig. 13: Parameters for Peak 9-13.

In summary, Ho-LGS exhibits a significantly different absorption spectrum compared to pure-LGS, particularly at frequencies of  $4800 \text{ cm}^{-1}$  and higher. The absorption peaks in the mid-infrared range, at frequencies of  $2300 - 3700 \text{ cm}^{-1}$ , are most likely attributed to elements such as La, Ga, Si or O within the crystal, rather than to the substitution of Ho. In this range, pure-LGS shows stronger absorption than Ho-LGS. At higher frequencies, the absorption intensity varies with polarization, with the  $\vec{E} \parallel c$  configuration showing greater absorbance than  $\vec{E} \perp c$ .

Almost all peaks exhibit the expected Boltzmann distribution behavior, showing a decrease in absorption amplitude with increasing temperature. The two exceptions are Peaks 6 & 9b, where a discontinuity in the absorption trend occurs at temperatures below 50 K. This deviation may result from spin-lattice coupling, though further investigation is required. All other peaks appear to result from electronic transitions or CEF excitations.

The following table summarizes the amplitude, frequency, and FWHM data for each addressed peak at 5 K. A more detailed discussion of peak behavior will be presented in the next chapter.

Peak Number	Frequency ( $\text{cm}^{-1}$ )	Amplitude ( $\text{m}^{-1}$ )	FWHM
<b>p-LGS <math>\vec{E} \parallel c</math></b>			
1	2347.738	50.743	7.068
2	2673.303	13.916	66.131
3a	2792.826	5.878	34.848
3b	2858.260	13.008	30.420
3c	2927.397	22.074	68.701
4	3417.631	120.992	73.974
5a	3689.376	21.061	18.978
5b	3726.113	18.537	8.103
<b>p-LGS <math>\vec{E} \perp c</math></b>			
1	2347.751	52.808	7.376
2	2690.177	20.729	122.012
3a	2856.648	13.922	29.131
3b	2932.553	21.355	65.621
4	3417.254	133.459	58.632
5a	3689.136	22.265	17.637
5b	3725.775	17.158	8.849
<b>Ho-LGS <math>\vec{E} \parallel c</math></b>			
1	2346.423	5.867	8.673
2	2687.204	7.203	151.324
3a	2799.323	4.409	60.848
3b	2848.363	7.587	13.044
3c	2920.991	11.041	106.674
4	3384.350	9.788	295.869
5a			
5b			
6	5120.961	350.604	18.797
7	8650.707	40.552	39.048
8	11197.660	8.045	13.144
9a	15549.800	216.751	90.253
9b	15715.470	352.977	78.651
10a	18555.973	147.834	147.226
10b	18647.029	243.684	62.252
10c	18729.244	289.241	80.933

Peak Number	Frequency (cm <sup>-1</sup> )	Amplitude (m <sup>-1</sup> )	FWHM
11a	20576.957	135.557	100.563
11b	20750.637	113.930	100.091
12	21174.194	86.803	85.369
13a	21385.105	130.867	62.393
13b	21493.949	80.007	93.188
<b>Ho-LGS <math>\vec{E} \perp c</math></b>			
1	2346.386	5.571	7.879
2	2687.622	5.958	115.262
3a			
3b	2848.377	9.188	10.716
3c	2926.468	8.710	62.909
4	3364.727	6.336	315.281
5a			
5b			
6	5122.015	316.003	17.999
7	8636.634	60.783	17.677
8	1126.771	5.163	59.413
9a	15559.902	55.153	109.616
9b	15713.503	41.167	94.020
10a	18553.251	119.397	132.433
10b	18649.748	76.184	58.354
10c	18731.706	34.115	70.278
11a	20576.071	82.905	58.784
11b	20726.795	34.147	89.502
12	21174.524	67.854	78.543
13a	21952.531	50.083	59.423
13b	21479.771	27.034	81.899

**Tab. 4:** All Peak Parameters at 5 K.

## 4 Discussion

The substitution of holmium (Ho) into langasite (LGS) crystals introduces unique optical properties to the system. The underlying physical properties and their effects will now be discussed.

The crystalline structures of pure-LGS and Ho-doped-LGS are expected to be nearly identical, as the substitution rate of Ho is only about 5%. In these crystals, phonon modes are concentrated in the low-frequency range, and this small concentration of Ho can cause slight shifts in the frequencies of some phonon modes [2]. However, in this study, the observed spectrum begins at  $2000\text{ cm}^{-1}$ , a range where additional phonon modes are not expected.

The substitution of holmium into the (pure) langasite crystal introduces partially filled f-orbitals to the system. The rare-earth element Ho brings 11 unpaired electrons in the 4f-subshell, which are well shielded by the outer 5s and 5p orbitals, with an electronic configuration of  $[Xe]4f^{11}5d^16s^2$ . This shielding localizes the 4f-electrons and reduces their involvement in chemical bonding, making them highly influential in holmium's magnetic and optical properties. Additionally, the crystal electric field (CEF), a static electric field created by the charge distribution of neighboring atoms, splits the otherwise degenerate energy levels of these 4f-electrons in this system. This splitting produces closely spaced sub-levels, allowing new low-energy transitions, known as CEF excitations, to occur [1].

Besides CEF excitations, electronic transitions play a significant role in the infrared absorption spectra. These transitions are not limited to the localized f-electrons and generally involve higher energy levels.

The absorption spectra of both langasite samples indicate that the optical interactions in the mid-infrared range of  $2300 - 3700\text{ cm}^{-1}$  are most likely not caused by the 4f-electrons of the substituted Ho, since the spectra show very similar behavior for both samples. Therefore, these absorption features are more likely caused by electronic transitions of other elements in the crystal, such as La, Ga, Si or O.

In the near-infrared range from  $8000 - 21600\text{ cm}^{-1}$ , numerous absorption features are observed for Ho-LGS. The closely spaced optical excitations and the occasional broadening of the absorption peaks suggest CEF excitations in this region. Another indication supporting this interpretation is that the pure-LGS sample does not show any of these optical events. Furthermore, as reported in [2], the dielectric permittivity along the *c*-axis is several times larger than that along the *a*- and *b*\*-axes, as confirmed by the higher absorption for the  $\vec{E} \parallel c$  configuration compared to  $\vec{E} \perp c$ , as shown in Fig. 12.

In addition to CEF excitations and electronic transitions, interactions between the lattice and the electronic system are also possible. This mechanism is referred to as spin-lattice coupling, the interaction between the electron spins and the phonons of the crystal lattice. This effect can cause anomalous behavior in site population and thus in the absorption peak behavior. In the observed spectrum of Ho-LGS, Peaks 6 & 9b exhibit such changes in peak parameters below temperatures of 50 K. Since there are no corresponding absorption features in the spectrum of pure-LGS, pure phonon modes can be excluded. However, to confirm this hypothesis, further analysis of this system's magnetic properties is needed.

The interpretation of the absorption spectra of pure-LGS and Ho-LGS provides insights into the CEF structure of the system. This is important for defining the electronic energy levels of the rare-earth system and understanding its magnetic and magneto-electric properties. The following

figure illustrates the CEF spectrum observed for Ho-LGS  $\vec{E} \parallel c$ , with the energy (frequency) data given in Tab. 4:

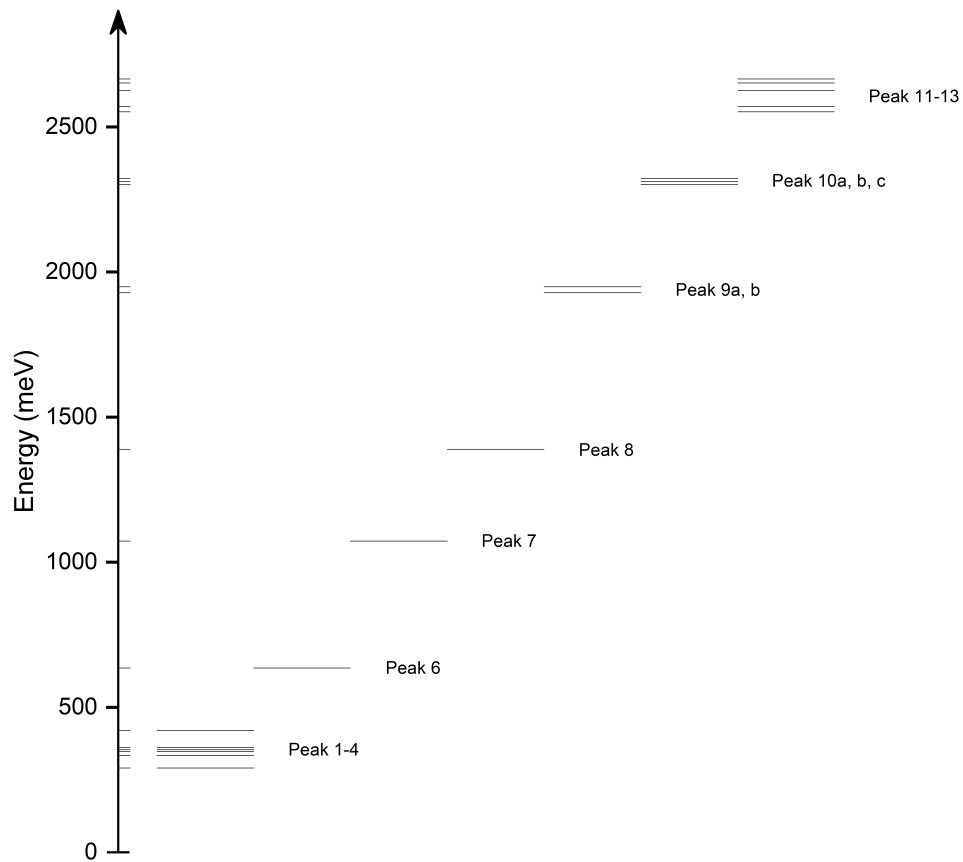


**Fig. 14:** CEF spectrum for Ho-LGS.

## 5 Conclusion

The crystal electric field (CEF) of pure and holmium-doped langasites (p-LGS and Ho-LGS) was investigated using FTIR transmission spectroscopy, with measurements conducted at low temperatures down to 5 K to capture the electronic ground states.

The absorption spectra indicate that Ho substitution significantly alters the magnetic and magnetoelectric properties of the crystal. Across the observed spectrum, Ho-LGS displays notable optical activity, while p-LGS shows no significant optical responses above frequencies of  $4800\text{ cm}^{-1}$ .

In the mid-infrared range, the observed absorption features in both samples appear to arise from other elements present in the crystal, such as La, Ga, Si or O, rather than the substitution of Ho. These pronounced electronic transitions may even originate from the ground state, contributing to the distinct absorption characteristics.

At higher frequencies, in the near-infrared range, Ho-LGS exhibits numerous absorption peaks consistent with CEF transitions. Additionally, the dielectric response along the c-axis is observed to be several times stronger than along the a- & b\*-axes, as indicated by the higher absorption intensity along this direction.

Several absorption peaks in Ho-LGS display unexpected behaviors below 50 K, deviating from typical electronic transitions or CEF excitations. These anomalies may be attributed to spin-lattice coupling, although further investigation, particularly magnetic measurements, is required to confirm this hypothesis.

Overall, this study provides a foundational survey of the CEF spectra in pure and Ho-doped langasites, enhancing the understanding of CEF effects and their influence on the ME properties. Specifically, several amplitude excitations suitable for testing non-reciprocal dichroism have been identified in the range from  $2250\text{ cm}^{-1}$  to  $21600\text{ cm}^{-1}$ , offering important preliminary results for future measurements under high magnetic fields. These insights lay the groundwork for further exploration of rare-earth-doped langasites in developing advanced optical devices, such as optical diodes.

## List of Figures

1	P321 Crystal structure of langasite, adapted from Ref. [2]. . . . .	3
2	Samples on Cryostat-Sample-Stick with Axis Label. . . . .	6
3	Transmission Reference of Bottom Place (Ho-LGS) at Room Temperature and with $\vec{E} \perp c$ . . . . .	6
4	Baseline Subtraction of p-LGS and Ho-LGS at 5K. . . . .	8
5	Full Transmission Spectra. . . . .	10
6	Full Attenuation-Coefficient Spectra. . . . .	11
7	Attenuation-Coefficient for 2300 - 3700 $\text{cm}^{-1}$ . . . . .	12
8	Parameters for Peak 1, 2, 3a, 3b, 3c & 4. . . . .	13
9	Attenuation-Coefficient for 4800 - 5400 $\text{cm}^{-1}$ . . . . .	14
10	Parameters for Peak 6. . . . .	14
11	Attenuation-Coefficient for 8000 - 11500 $\text{cm}^{-1}$ . . . . .	15
12	Attenuation-Coefficient for 14850 - 21600 $\text{cm}^{-1}$ . . . . .	16
13	Parameters for Peak 9-13. . . . .	17
14	CEF spectrum for Ho-LGS. . . . .	21

## References

- [1] D. Atwood. "The Rare Earth Elements: Fundamentals and Applications". In: *John Wiley and Sons Ltd* (2012).
- [2] L. Bergen, L. Weymann, J. Wettstein, A. M. Kuzmenko, A. A. Mukhin, B. V. Mill, A. Pimenov, and E. Constable. "Lattice contributions to the anisotropic dielectric response of rare-earth langasites". In: *Phys. Rev. B* (July 2021). DOI: 10.1103/PhysRevB.104.024106. URL: <https://link.aps.org/doi/10.1103/PhysRevB.104.024106>.
- [3] K. Kimura and T. Kimura. "Nonvolatile Switching of Large Nonreciprocal Optical Absorption at Shortwave Infrared Wavelengths". In: *Phys. Rev. Lett.* (Jan. 2024). DOI: 10.1103/PhysRevLett.132.036901. URL: <https://link.aps.org/doi/10.1103/PhysRevLett.132.036901>.
- [4] M. Kitaura, K. Mochizuki, Y. Inabe, M. Itoh, H. Nakagawa, and S. Oishi. "Fundamental optical properties and electronic structure of langasite  $\text{La}_3\text{Ga}_5\text{SiO}_{14}$  crystals". In: *Phys. Rev. B* (Mar. 2004). DOI: 10.1103/PhysRevB.69.115120. URL: <https://link.aps.org/doi/10.1103/PhysRevB.69.115120>.
- [5] T. Mayerhöfer, S. Pahlow, and J. Popp. "The Bouguer-Beer-Lambert Law: Shining Light on the Obscure." In: *Chemphyschem.* (Sept. 2020). DOI: 10.1002/cphc.202000464.
- [6] A. Y. Tikhanovskii, V. Y. Ivanov, A. M. Kuzmenko, A. Stunault, O. Fabelo, E. Ressouche, V. Simonet, R. Ballou, I. A. Kibalin, A. Pimenov, A. A. Mukhin, and E. Constable. "Resolving the local distortions of Ising-like moments in magnetoelectric Ho-doped langasite". In: *Phys. Rev. B* (June 2024). DOI: 10.1103/PhysRevB.109.214433. URL: <https://link.aps.org/doi/10.1103/PhysRevB.109.214433>.
- [7] L. Weymann, L. Bergen, T. Kain, A. Pimenov, A. Shuvaev, E. Constable, D. Szaller, B. V. Mill, A. M. Kuzmenko, V. Y. Ivanov, N. V. Kostyuchenko, A. I. Popov, A. K. Zvezdin, A. Pimenov, A. A. Mukhin, and M. Mostovoy. "Unusual magnetoelectric effect in paramagnetic rare-earth langasite". In: *npj Quantum Materials* (Sept. 2020). DOI: 10.1038/s41535-020-00263-9. URL: <http://dx.doi.org/10.1038/s41535-020-00263-9>.

## Appendix

Ho-LGS 00 Pol		Ho-LGS 90 Pol		p-LGS 00 Pol		p-LGS 90 Pol	
$\nu$ (cm <sup>-1</sup> )	$\alpha$ (m <sup>-1</sup> )	$\nu$ (cm <sup>-1</sup> )	$\alpha$ (m <sup>-1</sup> )	$\nu$ (cm <sup>-1</sup> )	$\alpha$ (m <sup>-1</sup> )	$\nu$ (cm <sup>-1</sup> )	$\alpha$ (m <sup>-1</sup> )
2254.07	145.65	2254.07	160.63	2044.67	371.72	1662.22	836.33
3784.36	175.17	3784.36	183.87	2067.02	356.61	2044.67	358.96
4649.68	185.98	4649.68	194.89	2105.11	340.11	2067.02	352.98
5549.10	194.94	5549.10	203.55	2141.54	328.81	2105.11	346.58
6947.25	203.21	6947.25	212.32	2200.74	315.81	2141.54	341.06
8157.84	209.24	8157.84	218.68	2247.99	310.09	2200.74	339.06
9274.65	215.29	9274.65	223.37	2297.25	309.17	2247.99	342.01
10536.40	218.09	10536.40	225.66	2393.36	311.96	2297.25	343.59
11900.45	221.58	11900.45	228.87	2415.08	313.79	2393.36	349.86
13405.16	226.54	13405.16	232.99	2458.91	314.08	2415.08	351.27
14760.68	229.80	14760.68	237.76	2493.97	317.50	2458.91	352.19
16205.72	234.61	16205.72	243.12	2527.17	318.57	2493.97	356.72
17053.99	236.11	17053.99	248.74	2546.25	318.41	2527.17	358.99
18230.82	243.58	17868.16	260.93	2581.52	321.56	2546.25	358.84
19036.12	255.17	19036.12	284.06	2738.47	348.37	2581.52	362.11
19598.79	258.10	19598.79	290.64	2828.94	358.84	2738.47	389.34
20046.37	262.55	20046.37	293.05	3000.01	378.22	2828.94	399.87
21638.61	270.44	21555.35	300.22	3043.26	384.38	3000.01	419.27
				3098.48	395.85	3043.26	425.64
				3144.90	407.38	3098.48	437.17
				3180.14	416.41	3144.90	448.76
				3267.11	437.14	3180.14	457.00
				3573.80	436.45	3267.11	477.75
				3649.33	433.72	3573.80	476.36
				3785.90	433.41	3649.33	473.25
				3894.72	429.54	3785.90	473.09
				4039.49	428.41	3894.72	469.55
				4168.40	435.91	4039.49	468.51
				4272.24	442.04	4168.40	476.09
				4643.35	457.33	4272.24	482.29
				5443.59	494.67	4643.35	498.14
				5903.73	516.72	5443.59	536.80
				7617.58	586.99	5903.73	559.91
				9158.04	639.26	7617.58	631.11
				10831.88	696.36	9158.04	685.77
				13119.23	765.98	10831.88	744.91
				14206.23	795.26	13119.23	816.98
				15333.23	821.85	14206.23	847.52
				16346.87	845.78	15333.23	874.56
				16787.00	856.47	16346.87	896.86
				17533.89	880.71	16787.00	917.91
				18340.80	917.71	17533.89	969.16
				18720.92	937.88	18340.80	1043.25
				19227.74	962.65	18720.92	1082.61
				19714.55	982.82	19227.74	1130.99
				20334.73	999.04	19714.55	1165.89

$\nu$ (cm <sup>-1</sup> )	$\alpha$ (m <sup>-1</sup> )	$\nu$ (cm <sup>-1</sup> )	$\alpha$ (m <sup>-1</sup> )	$\nu$ (cm <sup>-1</sup> )	$\alpha$ (m <sup>-1</sup> )	$\nu$ (cm <sup>-1</sup> )	$\alpha$ (m <sup>-1</sup> )
				21221.67	1021.96	20334.73	1195.98
				21995.23	1037.72	21221.67	1194.80
						21995.23	1199.18

**Tab. 5:** Anchor Points for the Baseline.